Low-level atmospheric turbulence dataset in China generated by combining radar wind profiler and radiosonde observations

Deli Meng[a, b], Jianping Guo[a,d*], Juan Chen[c], Xiaoran Guo[a], Ning Li[a], Yuping Sun[a], Zhen Zhang[a, e], Na Tang[a], Hui Xu[a], Tianmeng Chen[a], Rongfang Yang[f], Jiajia Hua[b]

[a]State Key Laboratory of Severe Weather Meteorological Science and Technology, Chinese Academy of Meteorological Sciences, Beijing 100081, China

[b]Xiong'an Atmospheric Boundary Layer Key Laboratory of China Meteorological Administration, Beijing 100085, China

[c]AVIC Leihua Electonic Technology Research Institute, Wuxi 214063, China

[d]Guizhou New Meteorological Technology Co., Ltd, Guiyang 550001, China

[e] Department of Atmospheric and Oceanic Sciences & Institute of Atmospheric Sciences, Fudan University, Shanghai 200438, China

[f]Hebei Meteorological Technology and Equipment Center, Shijiazhuang 050022, China

*Correspondence to: Dr/ Prof. Jianping Guo (Email: jpguocams@gmail.com)

Abstract

Low-level atmospheric turbulence plays a critical role in cloud dynamics and aviation safety. Nevertheless, altitude-resolved turbulence profiles remain scarce, largely owing to observational challenges. By leveraging collocated radar wind profiler (RWP) and radiosonde observations from 29 stations across China during 2023, a high vertical resolution dataset of low-level turbulence-related parameters are generated based on spectral width method. This dataset includes squared Brunt–Vaisala frequency (N^2), turbulent dissipation rate (ε), vertical eddy diffusivity (K), inner scale (l_0), and buoyancy length scale (L_B), which are provided twice daily at 00 and 12 UTC with a vertical resolution of 120 m, covering altitudes from 0.12 km to 3.0 km above ground level (AGL). Spatial analysis reveals significant regional disparities in turbulence-related parameters across China, where ε, K and L_B are higher in northwest and north China compared to south China, while N^2 and l_0 display an inverse spatial pattern. This contrasting geographical distributions suggest distinct atmospheric instability across China. In terms of seasonality, turbulence-related variables showed maxima during spring and summer. Vertical profiles characteristics show distinct altitudinal dependencies, ε, L_B and K exhibit progressive attenuation with altitude, while N^2 and l_0 increase with altitude. Statistical analysis indicates that ε and K follow log-normal distributions, whereas l_0 and L_B align with Gamma distributions. This dataset is publicly accessible https://doi.org/10.5281/zenodo.14959025 (Meng and Guo, 2025), which provides crucial insights into the fine-scale structural evolution of low-level turbulence. The preliminary findings based on the dataset have great implications for improving our understanding of pre-storm environment and conducting scientific planning and guiding of low-level flight routes in the emerging low-altitude economy in China.

Short Summary

This study provides a high vertical resolution dataset of low-level atmospheric turbulence across China, using radar and weather balloon observations. It reveals regional and seasonal variations in turbulence, with stronger activity in spring and summer. The dataset supports weather forecasting, aviation safety, and low-altitude flight planning, aiding China's growing low-altitude economy and accessible at https://doi.org/10.5281/zenodo.14959025.

1 Introduction

The low-level atmosphere below 3.0 km altitude serves as a critical interface for planetary boundary layer (PBL) and cloud interactions, and convective initiation processes (Marquis et al., 2021; Nowak et al., 2021). This dynamic transition zone facilitates exchange of water vapor, thermal energy, moment flux, and aerosol particles between Earth's surface and free atmosphere (Muñoz-Esparza et al., 2018; Brunke et al., 2022). The turbulence-driven exchanges can be quantitatively characterized by key physical parameters N^2, ε, K, l_0, L_B, and atmospheric refractive index structure constant (Cn^2) (Fukao et al., 1994; Wilson, 2004). These parameters collectively govern the energy cascade processes and momentum transfer mechanisms that dominate PBL thermodynamics. Accurately understanding the spatiotemporal evolution of low-level turbulence is crucial not only for improving predictive skill of severe convective systems through refined parameterization schemes but also implementing operational safeguards for low-altitude aviation safety.

Therefore, advances have been made in recent years in observational techniques for characterizing low-level turbulence. Conventional in-situ platforms include weather balloons (e.g., Clayson and Kantha, 2008; Guo et al., 2016; Kohma et al., 2019), rocket (Namboodiri et al., 2011) and aircraft (Nicholls et al., 1984; Brunke et al., 2022; Chechin et al., 2023). Concurrently, unmanned aerial vehicles (UAVs) have demonstrated growing potential in capturing low-level turbulence features that traditional aircraft and radiosonde networks cannot systematically resolve (Shelekhov et al., 2021). Nevertheless, these approaches face inherent limitations, such as high operational costs, discontinuous temporal sampling, and spatially constrained coverage limited to point measurements or linear transects. Such restrictions fundamentally impede the acquisition of vertically resolved turbulence profiles with sufficient spatiotemporal continuity.

To address these observational gaps, ground-based lidars and radars have emerged as pivotal solutions (Gage and Balsley, 1978). RWP and coherent Doppler wind lidar systems have demonstrated effectiveness in obtaining turbulence parameters with both high temporal resolution and operational continuity (Sato and Woodman, 1982; Hocking, 1985; Fukao et al., 1994; Nastrom and Eaton, 1997; Luce et al., 2023a; Meng et al., 2024).

ε, in conjunction with K, l_0, and L_B derivable from ε (Fukao et al., 1994), serve as critical determinants in radar-derived quantification of atmospheric turbulence metrics. Three principal methodological frameworks have emerged for retrieving ε in low-level atmosphere from RWP observations, namely the power method (Hocking, 1985; Hocking and Mu, 1997), variance method (Satheesan and Murthy, 2002), and Doppler spectral width method (Nastrom, 1997; Dehghan and Hocking, 2011). The power method utilizes backscattered signal intensity modulated by refractive index fluctuations (Weinstock, 1981a; Cohn, 1995). The variance method establishes a direct mathematical relationship between ε and the variance of vertical velocity (Satheesan and Murthy, 2002). Comprehensive reviews by Cohn (1995), Gage and Balsley (1978), and Wilson (2004) have thoroughly evaluated their underlying assumptions, advantages, and limitations. As highlighted by Satheesan and Murthy (2002), the power method necessitates thermodynamic profiles, the variance method demands accuracy in Doppler measurements, particularly challenged by contamination from non-turbulent motions in vertical beam observations, while the influence of ground clutter and the differences in the calculation of various spectral broadening terms are the main factors contributing to the large uncertainty in turbulence spectral width. Most widely adopted is the Doppler spectrum width technique, which isolates turbulence-induced spectral broadening through systematic removal of non-turbulent contributions (e.g., Cohn, 1995; Nastrom and Eaton, 1997; Eaton and Nastrom, 1998; Jacoby-Kaoly et al., 2002; Dehghan and Hocking, 2011; Kohma et al., 2019; Jaiswal et al., 2020; Solanki et al., 2022; Chen et al., 2022a, b; Luce et al., 2023b). The non-turbulent spectral widths are mainly contributed by beam broadening, shear effects, and gravity wave perturbations, which can be estimated by the algorithms proposed by Hocking (1985), Nastrom (1997), and Dehghan and Hocking (2011), respectively. Recent work by Chen et al. (2022b) identifies a critical vertical wind shear (VWS) threshold of 0.006 s^{-1}, beyond which turbulence spectral width retrievals become increasingly susceptible to negative value artifacts, highlighting unresolved challenges under extreme shear conditions that frequently accompany severe convective systems.

Complementing radar-based methodologies, the radiosonde measurements have been long used to derive the profiles of N^2 and ε using the Thorpe analysis method (Thorpe, 1977). Originally designed to diagnose turbulent overturning in the troposphere and lower stratosphere, this method enables cross-validation with radar-derived turbulence metrics through coordinated multi-platform campaigns (Clayson and Kantha, 2008; Wilson et al., 2014; Li et al., 2016; Kohma et al., 2019; Jaiswal et al., 2020; Lv et al., 2021; Rajput et al., 2022; Ko et al., 2024). Nevertheless, Thorpe analysis method is not suitable for the turbulence retrieval in the low-level atmosphere below 3.0 km AGL.

Even though significant stride has been made in calculating temporally continuous profiles of ε, other turbulence-related parameters such as l_0, L_B, and K in the low atmosphere remains insufficiently analyzed, particularly on a national scale, largely due to the lack of concurrent observations of high vertical resolution temperature, humidity and wind profiles. Fortunately, the RWP observational network has been built up and operated by China Meteorological Administration (CMA), and most of RWP stations are collocated with radiosonde stations. Furthermore, attempts were made to retrieve all the above-mentioned turbulence metrics by combining the measurements of RWP and radiosonde by Solanki et al. (2022). This motivates us to construct such low-level turbulence dataset in China, enabling a holistic view of the turbulence features throughout China. The paper is structed as follows. Section 2 details the data sources and methodology, including instrumentation specifications from the observational station and the retrieval method employed for turbulence-related parameters. Section 3 presents a multi-scale analysis of turbulence dynamics, encompassing vertical profile examinations and spatiotemporal variation patterns of low-level turbulence in China. Finally, summary and concluding remarks are given in Section 4.

2 Data and Methodology

2.1 RWP and radiosonde measurements

As of December 31, 2023, CMA operates a modern vertical meteorological observing network consisting of 120 L-band radiosonde and over 200 RWP stations. Through a rigorous station selection process, 29 optimally co-located observation stations were identified (Fig. 1) based on systematic evaluation of spatial representativeness and instrument performance metrics. These stations are equipped with an advanced RWP-radiosonde synergetic observation system specifically designed for retrieving low-level turbulence-related parameters. The network spans latitudes from 16.83°N to 49.22°N and longitudes from 75.98°E to 129.47°E, covering China's primary geomorphological regions, ranging from coastal plains (-0.4 m above mean sea level, AMSL) to high-mountain plateaus (4,326.8 m AMSL). Detailed station information is provided in Table 1.

The RWP system provides continuous wind profiling from 0.12 km to 5.0 km AGL, with a temporal resolution of 6 minutes and a vertical resolution of 120 m within the low-level atmosphere. The system incorporates advanced signal processing techniques, including ground clutter suppression algorithms and adaptive spectral filtering, to mitigate ground clutter interference and enhance real-time data fidelity (Solanki et al., 2022; Guo et al., 2023).

The L-band radiosonde system delivers high vertical resolution profiles with a temporal resolution of 1 second and a vertical resolution of 5–8 m. Routine observations are conducted twice daily at 00 UTC and 12 UTC. The radiosonde data undergo rigorous quality control and have been widely used in previous studies to examine spatiotemporal variations in turbulence and instability within the free atmosphere and PBL (Guo et al., 2016; Lv et al., 2021; Sun et al., 2025). Although horizontal displacement occurs between launch stations and balloon trajectories, the spatial exclusivity of these trajectories ensures non-overlapping sampling domains among stations. This spatial segregation, combined with high-density vertical profiling, enables statistically independent measurements of turbulence-related parameters at each station (Ko et al., 2024).

Prior to turbulence retrieval through RWP-radiosonde synergetic analysis, precipitation events were excluded using ground-based 1-minute precipitation observations. Profiles from the RWP and radiosondes were synchronized to a 6-minute time resolution, and data collected 30 minutes before and after precipitation events were excluded to minimize residual moisture effects on radar refractivity and balloon trajectory perturbations (Wu et al., 2024). This rigorous quality assurance process yielded 16,942 validated non-precipitation profiles, enabling statistically robust characterization of turbulence regimes across China.

2.2 Algorithms for the estimation of turbulence-related parameters

Figure 2 presents the flowchart illustrating the main steps involved in estimating the following turbulence-related parameters, N^2, ε, l_0, L_B, and K, respectively.

N^2 is usually used as a parameter which indicates stability of the stratification which has units of units s^{-2}, and can be estimated based on the pressure and temperature profiles from radiosonde measurement (Lilly et al., 1974):

$$N^2 = \frac{g}{\theta}\frac{\partial\theta}{\partial z} \tag{1}$$

where g (units: m^2 s^{-1}) is the gravitational acceleration, z (units: m) is the altitude AGL, and θ (units: K) is the potential temperature as follows:

$$\theta = T\left(\frac{1000}{P}\right)^{0.286} \tag{2}$$

where T (units: K) denotes temperature, P denotes pressure (units: hPa).

ε represents rate of energy cascading to smaller and smaller eddies until the energy is transformed into heat at the Kolmogorov scale (Fukao et al., 2014), which has units of units m^2 s^{-3}. ε can be estimated by the Doppler spectral width method (Nanstrom, 1997). Turbulent spectral broadening (σ_{turb}^2, units: m^2 s^{-2}) is quantified by deducting non-turbulent broadening components (i.e., beam broadening, shear broadening, and transient effects) from the observed spectral width (σ_{obs}^2, units: m^2 s^{-2}) (Dehghan and Hocking, 2011). The equation is as follows:

$$\sigma_{obs}^2 \approx \sigma_{turb}^2 + \sigma_{beam+shear}^2 \tag{3}$$

Beam and shear broading ($\sigma_{beam\_shear}^2$, units: m^2 s^{-2}) is calculated using the following equations (Dehghan and Hocking, 2011):

$$\sigma_{beam\_shear}^2 = \frac{\theta_{0.5}^2}{k} u^2 \cos\alpha - a_0 \frac{\theta_{0.5}}{k} \sin\alpha \left(u \frac{\partial u}{\partial z} \zeta\right) + b_0 \frac{2 \sin^2\alpha}{8k} \left(\frac{\partial u}{\partial z} \zeta\right)^2 + c_0 \sin^2\alpha \cos^2\alpha \, |u\xi| + d_0 \sin^2\alpha \cos^2\alpha \, \xi^2 \tag{4}$$

where $k = 4ln2$, $\zeta = 2R\theta_{0.5} \sin\alpha$, $\xi = \frac{\partial u}{\partial z} \frac{\Delta R}{\sqrt{12}}$, $a_0 = 0.945$, $b_0 = 1.500$, $c_0 = 0.030$, $d_0 = 0.825$ (Dehghan and Hocking, 2011). α is the beam zenith angle of the radar beam, $\theta_{0.5}$ is the radar half-power beam width, R is the radar radial sampling distance (units: m), ΔR is the radial distance resolution, Δz is the vertical resolution, u (units: m s^{-1}) is the horizontal wind speed at R_0, and $\frac{\partial u}{\partial z}$ (units: s^{-1}) is the VWS at R_0.

ε can be expressed as a function of turbulence-induced spectral broadening through the following relationship:

$$\varepsilon = \sigma_{turb}^3 \left(\frac{4\pi}{1.6}\right)^{3/2} J^{-3/2} \tag{5}$$

The term J (m$^{2/3}$) can be computed numerically with an estimate of the mean wind speed provided by RWP as follows：

$$J = 12\Gamma\left(\frac{2}{3}\right) \int_0^{\frac{\pi}{2}} d\varphi \int_0^{\frac{\pi}{2}} \sin^3\psi \left(b^2 \cos^2\psi + a^2 \sin^2\psi + \frac{L^2}{12} \sin^2\psi \cos^2\varphi\right)^{\frac{1}{3}} d\psi \tag{6}$$

where Γ is the gamma function, $a = \frac{R\,\theta_{0.5}}{4\sqrt{\ln 2}}$ is the radius of the pulse volume, $b = \frac{\Delta z}{8\sqrt{\ln 2}}$ is the half-length of the pulse, L is the product of the mean wind speed and dwell time of the RWP during the sampling time, which can be expressed as $u_t \Delta t$, and a, b, and L have units of meters. The double integration is taken between 0 and π/2 for both spherical coordinates ψ and φ (Solanki et al., 2022).

In the inertial subrange, l_0 (units: m) represents the scale for determining the transition region between the viscous and inertial subranges, and L_B (units: m) represents the scale for determining the transition region between the inertial and buoyancy subranges (Weinstock, 1978; Hocking, 1985; Fukao et al., 2014). L_B and l_0 can be computed as follows：

$$L_B = \frac{2\pi}{0.62}\left(\frac{\varepsilon}{N^3}\right)^{1/2} \tag{7}$$

$$l_0 = 7.4 \cdot (v^3/\varepsilon)^{1/4} \tag{8}$$

where v (units: m^2 s^{-1}) is the kinematic viscosity, $v = 2 * 10^{-5}/\rho$, and ρ represents atmospheric density which can be calculated based upon the pressure and temperature profiles measured by radiosonde (Eaton and Nastrom, 1998; Solanki et al., 2022).

K is the ratio of the kinematic heat flux to the mean potential temperature gradient (Weinstock, 1981b) which has units of units m^2 s^{-1}. K can be calculated from the following equation:

$$K = \gamma\varepsilon N^{-2} \tag{9}$$

where γ is the mixing efficiency, whose value is empirically determined varying between 0.2 and 1 (Fukao et al, 2014). $\gamma \approx Ri_f/(1 - Ri_f)$, where Ri_f is the flux Richardson number, an important parameter in turbulence that is indicative of the ratio of buoyancy production to shear production (Fukao et al, 2014). A value of 0.25 corresponding to $Ri_f = 0.20$ is used in this study (Clayson and Kantha, 2008).

3 Results and discussion

3.1 Horizontal distribution of turbulence-related parameters

The climatological analysis of low-level turbulence regime below 3.0 km AGL across China at 00 UTC and 12 UTC in 2023 (Fig. 3) reveals distinct spatial patterns in turbulence-related parameters. Those turbulence-related parameters contain gradient Richardson number (Ri) (Guo et al., 2016), N^2, ε, K, L_B, and l_0. To examine the regional changes in above-mentioned turbulence parameters, we divided China into four subregions, north China (NC), northwest China (NWC), south China (SC) and southwest China (SWC), respectively (Fig. 3a).

N^2 displays pronounced regional heterogeneity across China, characterized by enhanced static stability in SC and diminished stratification in NWC (Figs. 3a and 3b). This may be associated with the smaller Ri in NWC, indicating a more unstable atmospheric stratification (Figs. 3a-d). This instability may arise from intensified surface-atmosphere interactions driven by the unique environmental conditions over NWC, including elevated solar radiation flux due to reduced cloud cover, the predominance of bare soil and rock substrates with low albedo, and enhanced sensible heat flux from arid landscapes, as compared with those in SC (Xu et al., 2021). As can be seen from Figs. 3e and 3f, turbulence is stronger in NC and NWC compared to SC, by approximately 1 to 1.5 orders of magnitude, which may be related to stronger mechanical driven from VWS and thermally driven convective mixing from surface heating (Chen et al., 2022b). The K shows two-order amplification in NWC (Figs. 3g–h), governed by the synergistic enhancement of ε and N^2 through Equation 9. This contrasts with SC's suppressed turbulence regime, where higher vegetation density and moisture increase atmospheric stability (Guo et al., 2016; Xu et al., 2021).

For the two turbulence scales, L_B demonstrates inverse spatial patterns compared to l_0 (Figs. 3i–l). L_B shows larger values across NC, NWC, and SWC, contrasted by smaller values in SC. Equation 8 indicates that L_B is proportional to ε and inversely proportional to N^3, suggesting that smaller N^2 along with larger ε contributes to a larger value of L_B. In contrast, l_0 demonstrates an opposite distribution compared to L_B (Figs. 3i and 3j). Since l_0 is proportional to ρ^3 and inversely proportional to ε, lower ρ leads to larger l_0 values in SWC. As previously indicated, compared with SC, the strong sensible heat flux in NWC contributes to a more pronounced low-level turbulence characterized by larger L_B and smaller l_0 values.

Further analysis reveals that the climatological mean values for N^2 are $10^{-3.76}$ s^{-2} at 00 UTC and $10^{-3.88}$ s^{-2} at 12 UTC, while the corresponding values for Ri are 3.72 and 3.03, indicating greater atmospheric instability at 12 UTC. Under a more unstable atmosphere, turbulence is stronger at 12 UTC, with climatological values of $10^{-3.37}$ m^2 s^{-3}, $10^{0.72}$ m^2 s^{-1}, 240.5 m for ε, K and L_B, respectively. The enhancement in turbulence metrics at 12 UTC versus 00 UTC baseline originates from the delayed local solar noon in NWC (UTC+6 zones) compared to SC (UTC+8 zones). This leads to stronger turbulence (as shown in Figs. 3f, h) and larger maximum scale of eddy in the inertial subrange (Fig. 3l) in the NWC. Notably, low-level turbulence in SWC at 12 UTC exceeds those values in SC by ~25% (Figs. 3f, h, l), attributable to stronger surface heating over the Tibetan Plateau foothills and Taklamakan Desert.

3.2 Vertical structure and probability distribution function (PDF) characteristics of turbulence-related parameters

Figures 4a-f show the profiles of N^2, Ri, ε, l_0, L_B, and K at 12UTC on 16 July 2023, at Mingfeng in NWC, respectively. It is evident that the vertical structure characteristics of N^2 and Ri are similar (Figs. 4a and 4b). Below 1.0 km AGL, N^2 is lower than $10^{-4.60}$ s^{-2} (Fig. 4a), and Ri is lower than 0.5 (Fig. 4b) which suggesting static instability within low-level atmosphere. In the altitude range from 1.5 to 3.0 km AGL, Ri exceed 1, suggesting that an increase in static stability is a common feature. As shown in Figs. 4c-4e, ε, K, and L_B display consistent vertical structure below 3.0 km AGL, characterized by a pronounced decreasing trend with altitude. ε varies from $10^{-5.2}$ to $10^{-4.0}$ m^2 s^{-3} (Fig. 4c), while K ranges from $10^{-2.1}$ to $10^{0.5}$ m^2 s^{-1} (Fig. 4d) in the low-level atmosphere. L_B can reach up to about 600 m at 0.5 km but decreases to around 50 m at 3.0 km AGL (Fig. 4e). Conversely, l_0 increased with altitude, ranging from approximately 0.03 m at 0.5 km to about 0.06 m at 3.0 km AGL (Fig. 4f). Reduced stratification N^2 and Ri synergistically intensify turbulent mixing within the low-level atmosphere and result in larger eddies in the inertial subrange. Furthermore, the intensity of turbulent motions and L_B diminishes with altitude, while l_0 increases (Ghosh, 2003).

Figure 5 demonstrates the vertical stratification through stability parameters (N^2, Ri), turbulence characteristics (ε, K), and turbulence scales (l_0, L_B) within the low-level atmosphere in 2023 across China. Below 1.5 km AGL, the values of N^2 and Ri at 12 UTC are markedly lower than those at 00 UTC (Figs. 5a and 5b), reflecting enhanced atmospheric instability. $Log_{10}\varepsilon$ shows a nearly linear decrease with increasing altitude below 3.0 km (Fig. 5c), exhibiting gradients of $-10^{-3.70}$ m^2 s^{-3} km^{-1} at 00 UTC and -10$^-$

$^{3.68}$ m^2 s^{-3} km^{-1} at 12 UTC. This indicates stronger turbulence at lower altitudes, with minimal differences in decay rates. Aligned with ε, K decreases with altitude at rates of $-10^{-0.14}$ m^2 s^{-1} km^{-1} (00 UTC) and $-10^{0.33}$ m^2 s^{-1} km^{-1} (12 UTC), further supporting reduced turbulent mixing at higher altitudes (Fig. 5d). Larger values of L_B is observed at lower altitude, while the values of l_0 are larger at higher altitude (Figs. 5e, f) (Ghosh, 2003; Rajput et al., 2022). L_B decreases sharply with altitude, showing steeper gradients at 12 UTC (-180.6 m km^{-1}) compared to 00 UTC (-69.6 m km^{-1}), consistent with stronger turbulence (Fig. 5e). This logarithmic decline suggests rapid attenuation of large turbulent eddies with altitude. In contrast, l_0 increases with altitude at rates of 0.0083 m km^{-1} (00 UTC) and 0.0069 m km^{-1} (12 UTC), reflecting a shift toward smaller-scale turbulence between the viscous and inertial subranges at higher altitudes (Fig. 5f). Marked vertical variability in L_B and l_0 dynamics reveal turbulence-stratification coupling mechanisms.

Figure 6 presents the PDFs for low-level atmospheric stability parameters (N^2, Ri), turbulence metrics (ε, K), and turbulence scales (l_0, L_B). It can be observed that $Log_{10}N^2$ exhibit an approximately Beta-like distribution, with standard deviations of 10$^{-3.72}$ s^{-2} at 00 UTC and 10$^{-3.78}$ s^{-2} at 12 UTC (Fig. 6a). Ri displays characteristics of an approximate Gamma distribution (Fig. 6b), consistent with its sensitivity to shear-driven instabilities. Both ε and K show traits typical of log-normal distributions (Rajput et al., 2022), with standard deviations of 10$^{-3.11}$ m^2 s^{-3} (10$^{-3.07}$ m^2 s^{-3}) for ε, and 10$^{0.93}$ m^2 s^{-1} (10$^{1.09}$ m^2 s^{-1}) for K at 00UTC (12UTC), respectively (Figs. 6c-d). For the horizontal turbulence scale sizes, l_0 and L_B exhibit approximate Gamma distributions (Figs. 6e and 6f). l_0 exhibits standard deviations of 0.013 m (0.012 m) at 00 UTC (12 UTC), respectively. L_B displays larger variability deviations of 219.8 m (264.1 m) at 00 UTC (12 UTC), respectively. The distinct PDF shapes reflect fundamental differences in the statistical behavior of stability, turbulence, and mixing parameters. The near log-normal distributions of ε and K suggest Gaussian-like randomness in turbulent processes, while the Gamma and Beta-like distributions of Ri and $Log_{10}N^2$ align with their dependency on threshold-governed instabilities.

Figure 7 demonstrates the relationships among turbulence-related parameters, with their quantitative correlation coefficients systematically presented at 00 UTC and 12 UTC, respectively. Notably, $Log_{10}N^2$ and Ri exhibit strong covariation, reflecting progressive stratification breakdown during atmospheric destabilization. The correlation coefficients for $Log_{10}\varepsilon$ with $Log_{10}N^2$ at 00 UTC (Fig. 7a) and 12 UTC (Fig. 7b) are -0.19 and -0.13, while the coefficients with Ri are -0.22 and -0.12, respectively. These values suggest that turbulence tends to be stronger in unstable atmospheric regimes. $Log_{10}K$ demonstrates robust covariance with $Log_{10}\varepsilon$ (R>0.80), whereas inverse mechanistic linkages emerge stability indices ($Log_{10}N^2$ and Ri). L_B exhibits divergent relationships, showing positive correlations with turbulent metrics (R>0.65 with $Log_{10}\varepsilon$ and $Log_{10}K$), while displaying inverse correlations with stability indices (R<-0.45 with $Log_{10}N^2$ and Ri). The characteristic l_0 shows an inverse pattern to L_B, with negative correlations to $Log_{10}\varepsilon$ (R<-0.80) and $Log_{10}K$ (R<-0.60), but positive correlations with $Log_{10}N^2$ and Ri. The interaction manifests as a marked negative correlation between L_B and l_0, with statistical confirmation of their anticorrelation pattern. These systematic correlations collectively suggest that atmospheric stability of stratification in the buoyancy subrange fundamentally modulate turbulent cascades and energy transfer processes through their coordinated effects on both buoyancy-dominated and shear-driven turbulent structures (Lotfy et al., 2019; Rajput et al., 2022).

3.3 Seasonal variation of turbulence-related parameters with atmospheric stability

The previous subsection analyzed the spatial distribution and vertical structure of climatological turbulence-related parameters across China. This subsection focuses on the temporal turbulent variation in low-level atmosphere.

Figures. 8-9 systematically delineates interannual variability and seasonal cyclic patterns of N^2, Ri, ε, l_0, L_B, and K. N^2 is lower in spring and summer, but higher in autumn and winter, indicating greater atmospheric instability during warmer months (Figs. 8a and 8b, Fig. 9a). In summer, N^2 reaches its minimum below 1.2 km AGL, indicating a more unstable stratification. Both ε and K exhibit higher values in spring and summer, and lower values in autumn and winter, with an approximate increase of one order of magnitude during warmer seasons (Chen et al., 2022a) (Figs. 8c-f, Figs. 9c-d). L_B follows a similar seasonal pattern to ε and K (Figs. 8i-j, Fig. 9f), further supporting the link between turbulence intensity and turbulence scales in the buoyancy subrange. In contrast, the annual evolution of l_0 (Figs. 8g and 8h, Fig. 9e) is inversely related to ε and K, with smaller values in spring and summer and larger values in autumn and winter (Figs. 8g, 8h). The vertical profiles of ε, K, and L_B consistently decrease with altitude across all seasons, highlighting the altitude-dependent characteristics of turbulent processes.

The seasonal evolutions of ε at 00 UTC and 12 UTC are broadly similar, though ε is consistently stronger at 12 UTC, likely due to lower values of N^2 and Ri (Figs. 8a-b). In summer at 12 UTC, ε exceeds $10^{-3.5}$ $\mathrm{m^2\ s^{-3}}$ at an altitude of 1.8 km AGL, whereas in winter, this altitude is only reached at 0.6 km. This highlights the influence of seasonal turbulent dynamics on the development of the PBL. This suggests the existence of a maximum descent gradient region for ε and K at the PBL top (Meng et al., 2024). At 12 UTC, the l_0 values at 0.5 km are 0.012 m in summer and 0.013 m in winter, while at 1.2 km, those values are 0.021 m in summer and 0.024 m in winter, respectively (Fig. 8i). The values of L_B at 12 UTC are 910 m in summer and 550 m in winter at an altitude of 0.5 km, respectively (Fig. 8j). At 1.2 km, the values of L_B are 570 m in summer and 300 m in winter, respectively, which is approximately half of the values observed at 0.5 km. The seasonal variations in turbulence parameters underscore the critical role of atmospheric stability and PBL processes in modulating low-level turbulence intensity and mixing.

As previously discussed, the low-level atmosphere at 12 UTC exhibits greater instability compared to 00 UTC, resulting in stronger turbulence. However, it should be noted that 12 UTC corresponds to local standard time (LST) between 18 and 20, during which the PBL may exist in either a mixed or transitional state (Guo et al., 2016). To further investigate the relationship between turbulence structure and atmospheric stability at 12 UTC, this study adopted Ri<0.25 as an indicator of atmospheric instability (Chen et al., 2022a).

Figure 10 shows the vertical and seasonal distribution frequency of Ri<0.25 at 00 UTC and 12 UTC. A distinct seasonal variation in the occurrence frequency is observed. Analysis of the occurrence frequency climatology reveals pronounced seasonality in low-level instability, with peak intensity occurring and maximum eddies (L_B≈ 573.9 m) at 12 UTC in May during the spring-summer transition period dominated by enhanced thermal convection and synoptic-scale frontal activity (Chen et al., 2022a). This seasonal maximum coincides with weakened static stability and enhanced turbulence (Fig. 8), facilitating vigorous vertical mixing through buoyancy-driven plumes. Conversely, autumn-winter months exhibit suppressed turbulence and smaller L_B (minimum L_B ≈272.6 m in January), corresponding to increased atmospheric stratification and reduced surface heat fluxes under frequent temperature inversion regimes (Xu et al., 2021).

Furthermore, a significant discrepancy exists between the occurrence frequency of Ri<0.25 at 00 UTC and 12 UTC. For instance, in May, the vertical mean frequency of Ri<0.25 at 12 UTC is 23.6%, whereas at 00 UTC it registers only 14.9%. This disparity indicates a more unstable atmosphere and stronger turbulence at 12 UTC (Figs. 6d and 8c-f). Vertically, the frequency exhibits a decreasing trend with altitude, suggesting that the vertical structure of atmospheric instability contributes to the altitude-dependent attenuation of turbulence intensity (Figs. 5c-d and 8c-f).

Figure 11 presents the vertical structural distribution of correlations among turbulence-related parameters. $Log_{10}\varepsilon$ show positive correlations with occurrence frequency of Ri<0.25 across altitudes (Fig. 11a), though $Log_{10}K$ exhibits stronger correlations (not shown). This indicates that K responds more sensitively to unstable atmospheric instability, particularly at 12 UTC where the correlation coefficient exceeds 0.5 at 1.0−2.0 km AGL. As shown in Fig. 11b, l_0 demonstrates significant negative correlations (R<-0.90) with $Log_{10}\varepsilon$ vertically, suggesting that enhanced turbulence under lower atmospheric instability corresponds to smaller l_0 between the viscous and inertial subranges (Fig. 11b). Conversely, L_B show significant positive correlations with $Log_{10}\varepsilon$, implying that stronger turbulence enlarges the maximum turbulent eddies between the inertial and buoyancy subranges (Fig. 11c). The correlation between l_0 and L_B is more pronounced at lower altitudes but remains relatively stable above 1.0 km. Hence, when the instability of the low-level atmosphere increases, the enhanced turbulence expands the range of the inertial subrange (Rajput et al., 2022).

4 Summary and concluding remarks

The estimation of turbulence-related parameters can help improving the accuracy of short-term local weather forecasts. Despite its importance, detailed research on the structure of low-level atmospheric turbulence has been hindered by a lack of comprehensive observational data. This study aims to address this gap by investigating the temporal and spatial evolution patterns of low-level turbulence in China.

Using observational data from 29 co-located RWP and radiosonde stations across China, this research employs the Doppler spectrum width method to estimate critical parameters of lower-level atmospheric turbulence. These parameters include the N^2, ε, l_0, L_B, and K. A comprehensive dataset of turbulence-related parameters was developed at the station scale for China in 2023, with a temporal resolution of 6-minute and a vertical resolution of 120 m below 3.0 km AGL.

Spatially, low-level turbulence demonstrates significant geographical variability. Compared to SC, N^2 and l_0 are lower in NWC and NC, while ε, L_B, and K are higher. This indicates stronger turbulence in the NWC and NC. It can be concluded that the predominance of bare land with low soil moisture in NWC and NC results in higher sensible heat flux, promoting greater heat transfer to the PBL, more unstable atmospheric stratification, and stronger turbulence compared to the forested, high soil moisture regions of SC.

As altitude increases, ε, L_B, and K exhibit a decreasing trend, while N^2 and l_0 increase. The PDF of ε and K conform a log-normal distribution, whereas l_0 and L_B approximately follow a Gamma distribution. Temporally, turbulence-related parameters display pronounced seasonal variations, with stronger turbulence observed in spring and summer and weaker turbulence in autumn and winter. Additionally, turbulence intensity at 12 UTC is notably stronger than at 00 UTC, primarily due to the unstable atmospheric stratification with a larger occurrence frequency of Ri<0.25.

Although the dataset of low-level atmospheric turbulence-related parameters developed in this study encompasses typical regions across China, the limited station density and sparse radiosonde observations constrain the dataset's ability to provide high spatiotemporal resolution turbulence profiles for the entire country. In future work, additional data sources, such as coherent Doppler wind lidars and reanalysis datasets, will be integrated to construct a more refined, grid-scale turbulence dataset for China, enabling a more comprehensive understanding of atmospheric turbulence dynamics.

Author contributions

JG designed the research framework and conceptualized this study; DM and JG conducted the experiment and drafted the initial manuscript; XG, NL and NT helped the data collection and carried out the quality control. YS and ZZ prepared all distributed turbulence-related datasets. JC, HX, TC, JH and RY contributed to the revision of the manuscript. All authors contributed to writing and reviewing the paper.

Competing interests

The contact author has declared that there are no competing interests for all authors.

Financial support

This manuscript was jointly under the auspices of the National Natural Science Foundation of China under grants of 42325501, the Chinese Academy of Meteorological Sciences under grant 2024Z003 and the Department of Science and Technology of Guizhou province under grant KXJZ [2024] 033. the CMA Xiong’an Atmospheric Boundary Layer Key Laboratory under grant of 2023LABL-B06.

Data availability

The low-level turbulence-related dataset in China can be accessed at https://doi.org/10.5281/zenodo.14959025 (Meng and Guo, 2025).

References

Brunke, M. A., Cutler, L., Urzua, R. D., Corral, A. F., Crosbie, E., Hair, J., Hostetler, C., Kirschler, S., Larson, V., Li, X. Y., Ma, P. L., Minke, A., Moore, R., Robinson, C. E., Scarino, A. J., Schlosser, J., Shook, M., Sorooshian, A., Thornhill, K. L., Voigt, C., Wan, H., Wang, H. L., Winstead, E., Zeng, X. B., Zhang, S. X., and Ziemba, L. D.: Aircraft observations of turbulence in cloudy and cloud-free boundary layers over the western north Atlantic ocean from ACTIVATE and implications for the earth system model evaluation and development, J. Geophys. Res.-Atmos., 127, 24, 10.1029/2022jd036480, 2022.

Chechin, D. G., Lüpkes, C., Hartmann, J., Ehrlich, A., and Wendisch, M.: Turbulent structure of the Arctic boundary layer in early summer driven by stability, wind shear and cloud-top radiative cooling: ACLOUD airborne observations, Atmos. Chem. Phys., 23, 4685-4707, 10.5194/acp-23-4685-2023, 2023.

Chen, Z., Tian, Y. F., and Lue, D. R.: Turbulence parameters in the troposphere-lower stratosphere observed by Beijing MST radar, Remote Sens., 14, 18, 10.3390/rs14040947, 2022a.

Chen, Z., Tian, Y. F., Wang, Y. A., Bi, Y. H., Wu, X., Huo, J., Pan, L. J., Wang, Y., and Lü, D. R.: Turbulence parameters measured by the Beijing mesosphere-stratosphere-troposphere radar in the troposphere and lower stratosphere with three models: comparison and analyses, Atmos. Meas. Tech., 15, 4785-4800, 10.5194/amt-15-4785-2022, 2022b.

Clayson, C. A. and Kantha, L.: On turbulence and mixing in the free atmosphere inferred from high-resolution soundings, J. Atmos. Ocean. Technol., 25, 833-852, 10.1175/2007jtecha992.1, 2008.

Cohn, S. A.: Radar Measurements of Turbulent eddy dissipation rate in the troposphere a comparison of techniques, J. Atmos. Ocean. Technol., 12, 85-95, 10.1175/1520-0426(1995)012<0085:Rmoted>2.0.Co;2, 1995.

Dehghan, A. and Hocking, W. K.: Instrumental errors in spectral-width turbulence measurements by radars, J. Atmos. Sol.-Terr. Phys., 73, 1052-1068, 10.1016/j.jastp.2010.11.011, 2011.

Eaton, F. D. and Nastrom, G. D.: Preliminary estimates of the vertical profiles of inner and outer scales from White Sands Missile Range, New Mexico, VHF radar observations, Radio Sci., 33, 895-903, 10.1029/98rs01254, 1998.

Fukao, S., Hamazu, K., and Doviak, R. J.: Radar for meteorological and atmospheric observations, Springer, 10.1007/978-4-431-54334-3, 2014.

Fukao, S., Yamanaka, M. D., Ao, N., Hocking, W. K., Sato, T., Yamamoto, M., Nakamura, T., Tsuda, T., and Kato, S.: Seasonal variability of vertical eddy diffusivity in the middle atmosphere 1. Three-year observations by the middle and upper atmosphere radar, J. Geophys. Res.-Atmos., 99, 18973-18987, 10.1029/94jd00911, 1994.

Gage, K. S. and Balsley, B. B.: Doppler radar probing of the clear atmosphere, Bull. Amer. Meteorol. Soc., 59, 1074-1093, 10.1175/1520-0477(1978)059<1074:Drpotc>2.0.Co;2, 1978.

Ghosh, A. K., Jain, A. R., and Sivakumar, V.: Simultaneous MST radar and radiosonde measurements at Gadanki (13.5°N, 79.2°E) 2. Determination of various atmospheric turbulence parameters, Radio Sci., 38, 12, 10.1029/2000rs002528, 2003.

Guo, J. P., Miao, Y. C., Zhang, Y., Liu, H., Li, Z. Q., Zhang, W. C., He, J., Lou, M. Y., Yan, Y., Bian, L. G., and Zhai, P.: The climatology of planetary boundary layer height in China derived from radiosonde and reanalysis data, Atmos. Chem. Phys., 16, 13309-13319, 10.5194/acp-16-13309-2016, 2016.

Hocking, W. K.: Measurement of turbulent energy dissipation rates in the middle atmosphere by radar techniques A review, Radio Sci., 20, 1403-1422, 10.1029/RS020i006p01403, 1985.

Hocking, W. K. and Mu, P. K. L.: Upper and middle tropospheric kinetic energy dissipation rates from measurements of (Cn^2)over-bar - review of theories, in-situ investigations, and experimental studies using the Buckland Park atmospheric radar in Australia, J. Atmos. Sol.-Terr. Phys., 59, 1779-1803, 10.1016/s1364-6826(97)00020-5, 1997.

Jacoby-Koaly, S., Campistron, B., Bernard, S., Bénech, B., Girard-Ardhuin, F., Dessens, J., Dupont, E., and Carissimo, B.: Turbulent dissipation rate in the boundary layer via UHF wind profiler Doppler spectral width measurements, Bound.-Layer Meteor., 103, 361-389, 10.1023/a:1014985111855, 2002.

Jaiswal, A., Phanikumar, D. V., Bhattacharjee, S., and Naja, M.: Estimation of turbulence parameters using aries st radar and gps radiosonde measurements: first results from the central himalayan region, Radio Sci., 55, 18, 10.1029/2019rs006979, 2020.

Ko, H. C., Chun, H. Y., Geller, M. A., and Ingleby, B.: Global distributions of atmospheric turbulence estimated using operational high vertical-resolution radiosonde data, Bull. Amer. Meteorol. Soc., 105, E2551-E2566, 10.1175/bams-d-

23-0193.1, 2024.

Kohma, M., Sato, K., Tomikawa, Y., Nishimura, K., and Sato, T.: Estimate of turbulent energy dissipation rate from the VHF radar and radiosonde observations in the Antarctic, J. Geophys. Res.-Atmos., 124, 2976-2993, 10.1029/2018jd029521, 2019.

Li, Q., Rapp, M., Schrön, A., Schneider, A., and Stober, G.: Derivation of turbulent energy dissipation rate with the Middle Atmosphere Alomar Radar System (MAARSY) and radiosondes at Andoya, Norway, Ann. Geophys., 34, 1209-1229, 10.5194/angeo-34-1209-2016, 2016.

Lilly, D. K., Waco, D. E., and Adelfang, S. I.: Stratospheric mixing estimated from high-altitude turbulence measurements, J. Appl. Meteorol., 13, 488-493, 10.1175/1520-0450(1974)013<0488:Smefha>2.0.Co;2, 1974.

Lotfy, E. R., Abbas, A. A., Zaki, S. A., and Harun, Z.: Characteristics of turbulent coherent structures in atmospheric flow under different shear-buoyancy conditions, Bound.-Layer Meteor., 173, 115-141, 10.1007/s10546-019-00459-y, 2019.

Luce, H., Kantha, L., and Hashiguchi, H.: Statistical assessment of a Doppler radar model of TKE dissipation rate for low Richardson numbers, Atmos. Meas. Tech., 16, 5091-5101, 10.5194/amt-16-5091-2023, 2023a.

Luce, H., Kantha, L., Hashiguchi, H., Lawrence, D., Doddi, A., Mixa, T., and Yabuki, M.: Turbulence kinetic energy dissipation rate: assessment of radar models from comparisons between 1.3 GHz wind profiler radar (WPR) and DataHawk UAV measurements, Atmos. Meas. Tech., 16, 3561-3580, 10.5194/amt-16-3561-2023, 2023b.

Lv, Y. M., Guo, J. P., Li, J., Cao, L. J., Chen, T. M., Wang, D., Chen, D. D., Han, Y., Guo, X. R., Xu, H., Liu, L., Solanki, R., and Huang, G.: Spatiotemporal characteristics of atmospheric turbulence over China estimated using operational high-resolution soundings, Environ. Res. Lett., 16, 13, 10.1088/1748-9326/abf461, 2021.

Muñoz-Esparza, D., Sharman, R. D., and Lundquist, J. K.: Turbulence dissipation rate in the atmospheric boundary layer: observations and WRF mesoscale modeling during the XPIA field campaign, Mon. Weather Rev., 146, 351-371, 10.1175/mwr-d-17-0186.1, 2018.

Marquis, J. N., Varble, A. C., Robinson, P., Nelson, T. C., and Friedrich, K.: Low-level mesoscale and cloud-scale interactions promoting deep convection initiation, Mon. Weather Rev., 149, 2473-2495, 10.1175/mwr-d-20-0391.1, 2021.

Namboodiri, K. V. S., Dileep, P. K., Mammen, K., Ramkumar, G., Kumar, N., Sreenivasan, S., Kumar, B. S., and Manchanda, R. K.: Effects of annular solar eclipse of 15 January 2010 on meteorological parameters in the 0 to 65 km region over Thumba, India, Meteorol. Z., 20, 635-647, 10.1127/0941-2948/2011/0253, 2011.

Nicholls, S.: The dynamics of stratocumulus Aircraft observations and comparisons with a mixed layer model, Q. J. R. Meteorol. Soc., 110, 783-820, 10.1002/qj.49711046603, 1984.

Nowak, J. L., Siebert, H., Szodry, K. E., and Malinowski, S. P.: Coupled and decoupled stratocumulus-topped boundary layers: turbulence properties, Atmos. Chem. Phys., 21, 10965-10991, 10.5194/acp-21-10965-2021, 2021.

Meng, D., Guo, J.: A low-level turbulence-related parameters dataset derived from the radar wind profiler and radiosonde in China during 2023. [Data set]. https://doi.org/10.5281/zenodo.14959025, 2025.

Meng, D. L., Guo, J. P., Guo, X. R., Wang, Y. J., Li, N., Sun, Y. P., Zhang, Z., Tang, N., Li, H. R., Zhang, F., Tong, B., Xu, H., and Chen, T. M.: Elucidating the boundary layer turbulence dissipation rate using high-resolution measurements from a radar wind profiler network over the Tibetan Plateau, Atmos. Chem. Phys., 24, 8703-8720, 10.5194/acp-24-8703-2024, 2024.

Nastrom, G. D.: Doppler radar spectral width broadening due to beamwidth and wind shear, Ann. Geophys.-Atmos. Hydrospheres Space Sci., 15, 786-796, 10.1007/s00585-997-0786-7, 1997.

Nastrom, G. D. and Eaton, F. D.: A brief climatology of eddy diffusivities over White Sands Missile Range, New Mexico, Journal of Geophysical Research-Atmospheres, 102, 29819-29826, 10.1029/97jd02208, 1997.

Rajput, A., Singh, N., Singh, J., and Rastogi, S.: Investigation of atmospheric turbulence and scale lengths using radiosonde measurements of GVAX-campaign over central Himalayan region, J. Atmos. Sol.-Terr. Phys., 235, 16, 10.1016/j.jastp.2022.105895, 2022.

Satheesan, K. and Murthy, B. V. K.: Turbulence parameters in the tropical troposphere and lower stratosphere, Journal of Geophysical Research-Atmospheres, 107, 13, 10.1029/2000jd000146, 2002.

Sato, T. and Woodman, R. F.: Fine altitude resolution observations of stratospheric turbulent layers by the Arecibo 430-MHz radar, J. Atmos. Sci., 39, 2546-2552, 10.1175/1520-0469(1982)039<2546:Faroos>2.0.Co;2, 1982.

Shelekhov, A. P., Afanasiev, A. L., Shelekhova, E. A., Kobzev, A. A., Tel'minov, A. E., Molchunov, A. N., and Poplevina, O. N.: Using small unmanned aerial vehicles for turbulence measurements in the atmosphere, Izv. Atmos. Ocean. Phys., 57, 533-545, 10.1134/s0001433821050133, 2021.

Solanki, R., Guo, J. P., Lv, Y. M., Zhang, J., Wu, J. Y., Tong, B., and Li, J.: Elucidating the atmospheric boundary layer turbulence by combining UHF radar wind profiler and radiosonde measurements over urban area of Beijing, Urban CLim., 43, 13, 10.1016/j.uclim.2022.101151, 2022.

Sun, Y., Guo J., Chen T., Li N., Guo X., Xu H., Zhang Z., Shi Y., Zeng L., Chen J., Meng D.: Long-term high-resolution radiosonde measurements reveal more intensified and frequent turbulence at cruising altitude in China, Geophys. Res. Lett., 52, e2024GL114076, /10.1029/ 2024GL114076, 2025.

Thorpe, S. A.: Turbulence and mixing in a Scottish Loch, Philos. Trans. R. Soc. A-Math. Phys. Eng. Sci., 286, 125-181, 10.1098/rsta.1977.0112, 1977.

Weinstock, J.: Vertical turbulent diffusion in a stably stratified fluid, J. Atmos. Sci., 35, 1022-1027, 10.1175/1520-0469(1978)035<1022:Vtdias>2.0.Co;2, 1978.

Weinstock, J.: Using radar to estimate dissipation rates in thin layers of turbulence, Radio Sci., 16, 1401-1406, 10.1029/RS016i006p01401, 1981a.

Weinstock, J.: Vertical turbulence diffusivity for weak or strong stable stratification, J. Geophys. Res.-Oceans., 86, 9925-9928, 10.1029/JC086iC10p09925, 1981b.

Wilson, R.: Turbulent diffusivity in the free atmosphere inferred from MST radar measurements: a review, Ann. Geophys., 22, 3869-3887, 10.5194/angeo-22-3869-2004, 2004.

Wilson, R., Luce, H., Hashiguchi, H., Nishi, N., and Yabuki, Y.: Energetics of persistent turbulent layers underneath mid-level clouds estimated from concurrent radar and radiosonde data, J. Atmos. Sol.-Terr. Phys., 118, 78-89, 10.1016/j.jastp.2014.01.005, 2014.

Wu, J. Y., Guo, J. P., Yun, Y. X., Yang, R. F., Guo, X. R., Meng, D. L., Sun, Y. P., Zhang, Z., Xu, H., and Chen, T. M.: Can ERA5 reanalysis data characterize the pre-storm environment? Atmos. Res., 297, 18, 10.1016/j.atmosres.2023.107108, 2024.

Xu, Z. Q., Chen, H. S., Guo, J. P., and Zhang, W. C.: Contrasting effect of soil moisture on the daytime boundary layer under different thermodynamic conditions in summer over China, Geophysical Research Letters, 48, 11, 10.1029/2020gl090989, 2021.

Table 1. Summary of the radar wind profiler (RWP) stations used in the calculation of turbulence related parameters.

ID	Station	Lon. (°E)	Lat. (°N)	Elevation (m)
50953	Harbin	126.58	45.93	115.0
51463	Urumqi	87.74	43.81	935.0
51839	Minfeng	82.69	37.07	1408.9
52533	Jiuquan	98.49	39.77	1477.2
53463	Hohhot	111.57	40.86	1152.1
53772	Taiyuan	112.58	37.62	785.0
53845	Yan'an	109.45	36.58	1180.4
54304	Zhangjiakou	115.27	40.95	726.0
54511	Beijing	116.47	39.81	31.5
54727	Zhangqiu	117.52	36.65	251.9
55664	Tingri	87.12	28.65	4326.8
56029	Yushu	96.96	33.00	3684.0
56146	Ganzi	100.00	31.62	3353.0
56173	Hongyuan	102.55	32.79	3465.0
56312	Linzhi	94.36	29.65	2988.4
56651	Lijiang	100.22	26.85	2382.4
56964	Simao	100.99	22.82	1423.3
57461	Sanxia	111.36	30.74	253.8
57516	Chongqing	106.46	29.58	260.0
57687	Changsha	112.79	28.11	46.0
57816	Guiyang	106.73	26.59	1223.7
58238	Nangjing	118.90	31.93	40.6
58459	Hangzhou	120.29	30.18	43.0
58633	Quzhou	118.89	28.99	86.4
58725	Shaowu	117.50	27.31	363.6
58847	Fuzhou	119.29	26.08	112.1
59312	Chaozhou	116.69	23.67	7.0
59431	Nanning	108.55	22.78	104.9
59758	Haikou	110.25	19.99	69.0

Figures

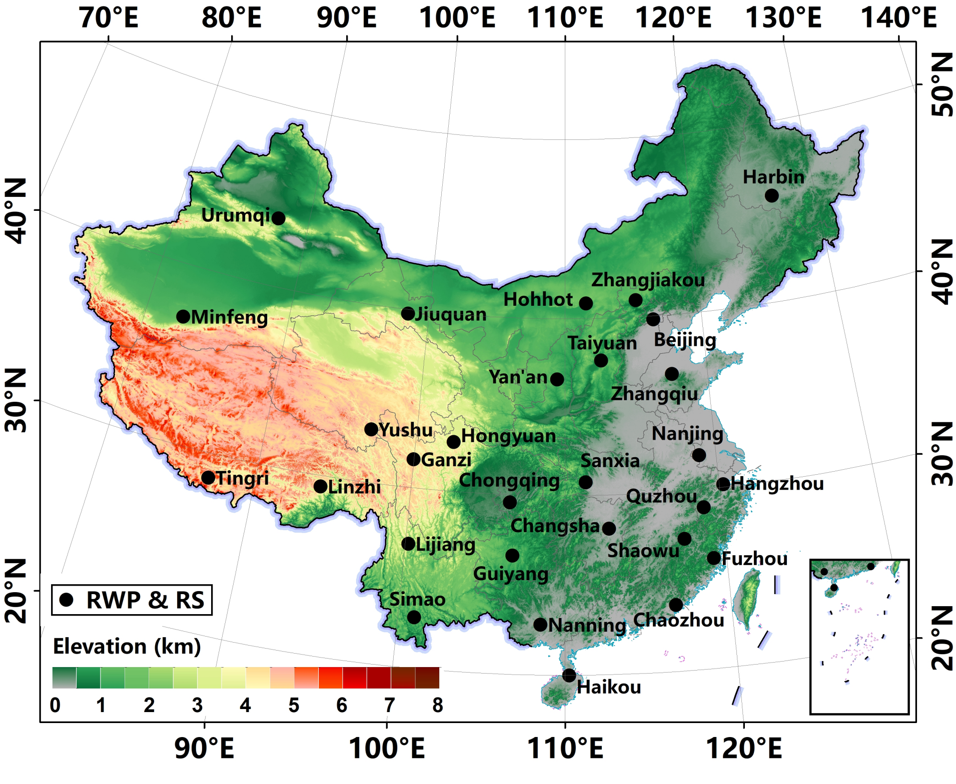

Figure 1. Spatial distribution of the co-located radar wind profiler (RWP) and radiosonde stations in China.

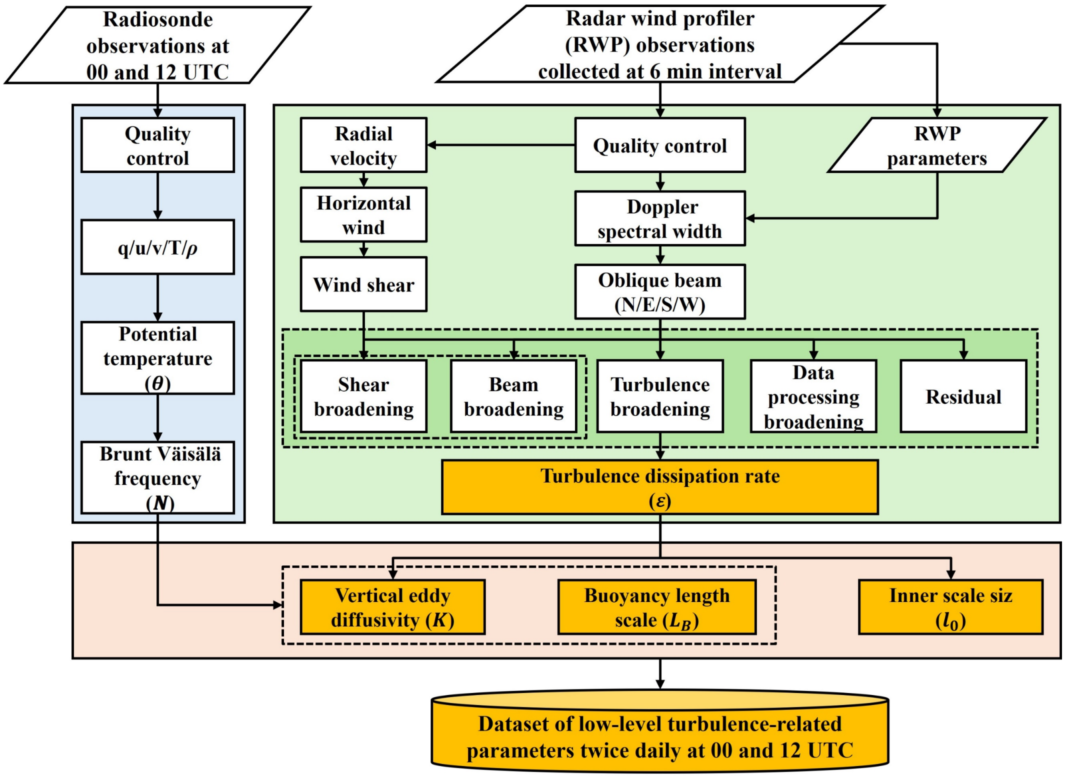

Figure 2. Flowchart used to generate the low-level atmospheric turbulence-related dataset at 00 UTC and 12 UTC in China. Turbulence-related parameters include squared Brunt Vaisala frequency (N^2), turbulent dissipation rate (ε), inner scale (l_0), buoyancy length scale (L_B), vertical eddy diffusivity (K), respectively.

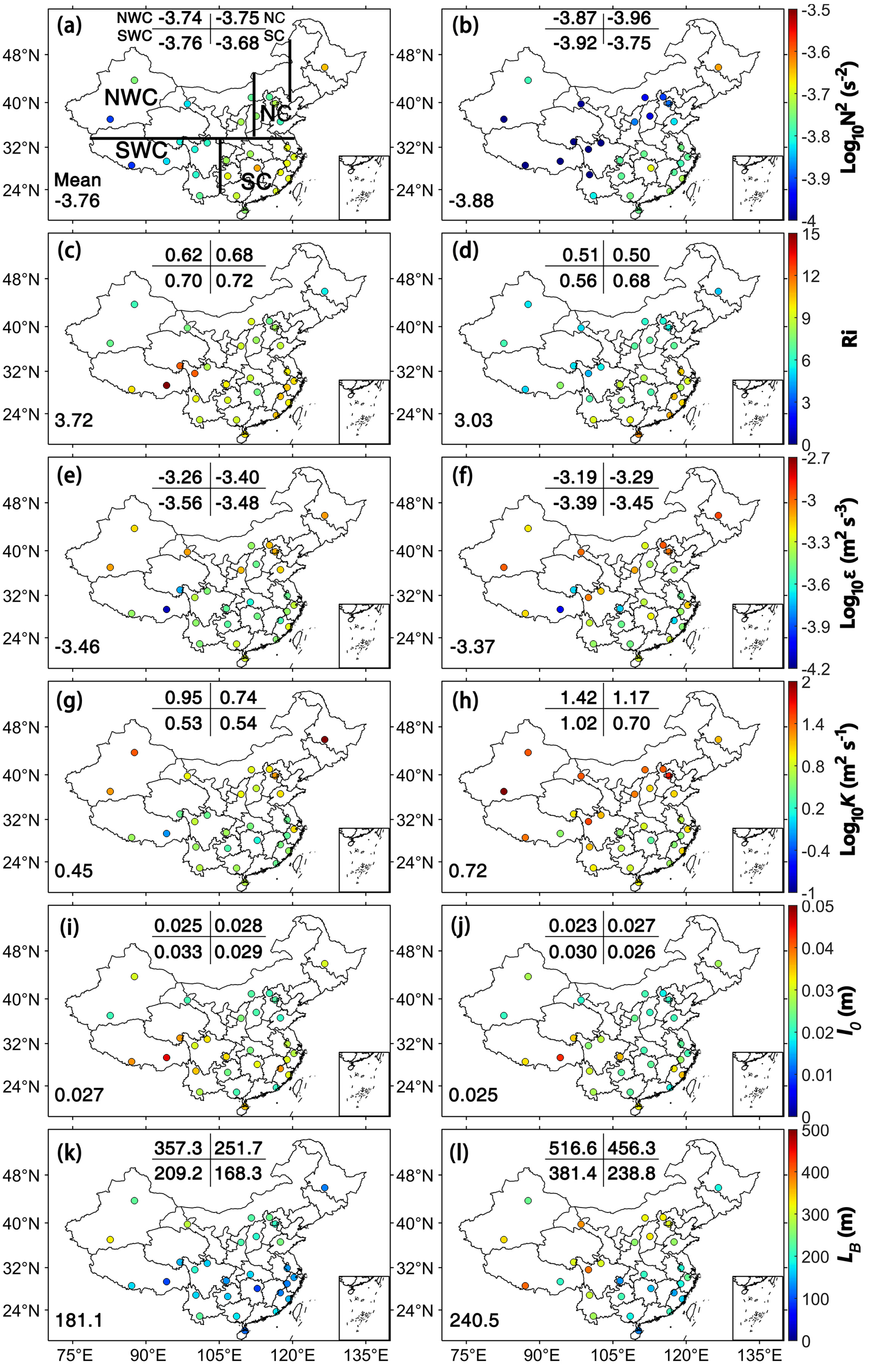

Figure 3. Spatial distribution and mean values of N^2 below 3.0 km above ground level (AGL) for 2023 at (a) 00 UTC and (b) 12 UTC, (c, d) Ri, (e, f) ε, (g, h) K, (i, j) l_0, (k, l) L_B, respectively. Here, China is divided into four subregions, north China (NC), northwest China (NWC), south China (SC) and southwest China (SWC), respectively.

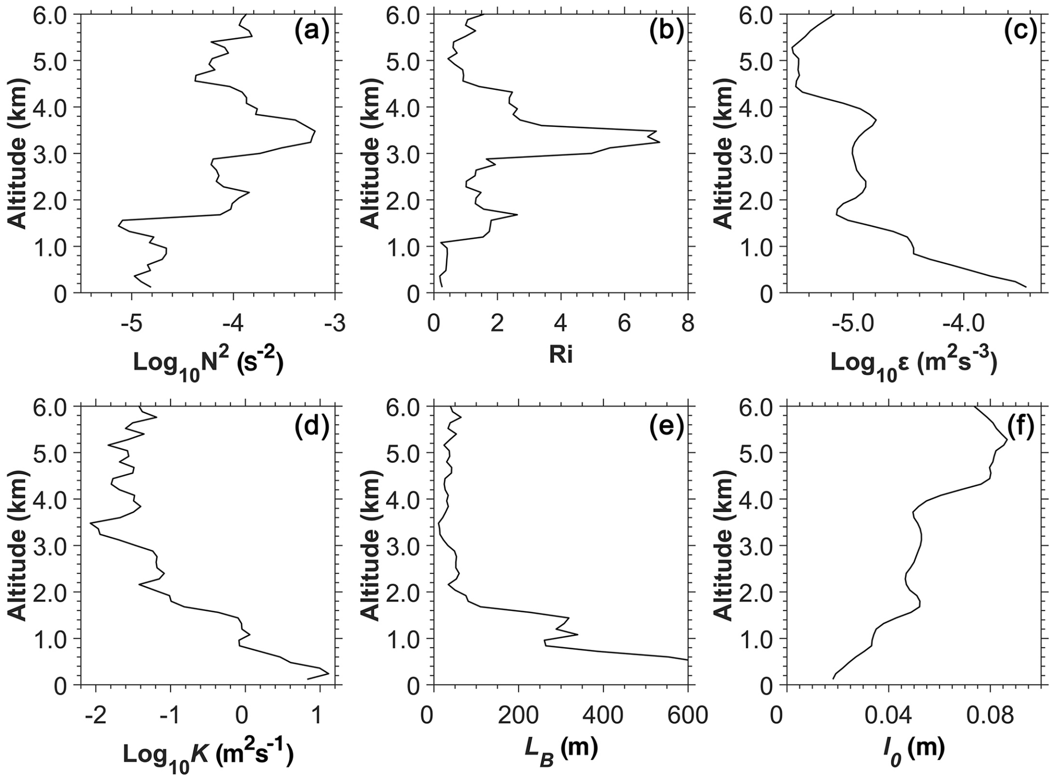

Figure 4. Vertical profiles of (a) N^2, (b) Ri, (c) ε, (d) K, (e) L_B and (f) l_0 at 12 UTC for 16 July 2023 at Minfeng in northwest China. Note that N^2 is deduced from the sorted θ, it shows no regions of negative stability, however, Ri is inferred from the unsorted θ profile.

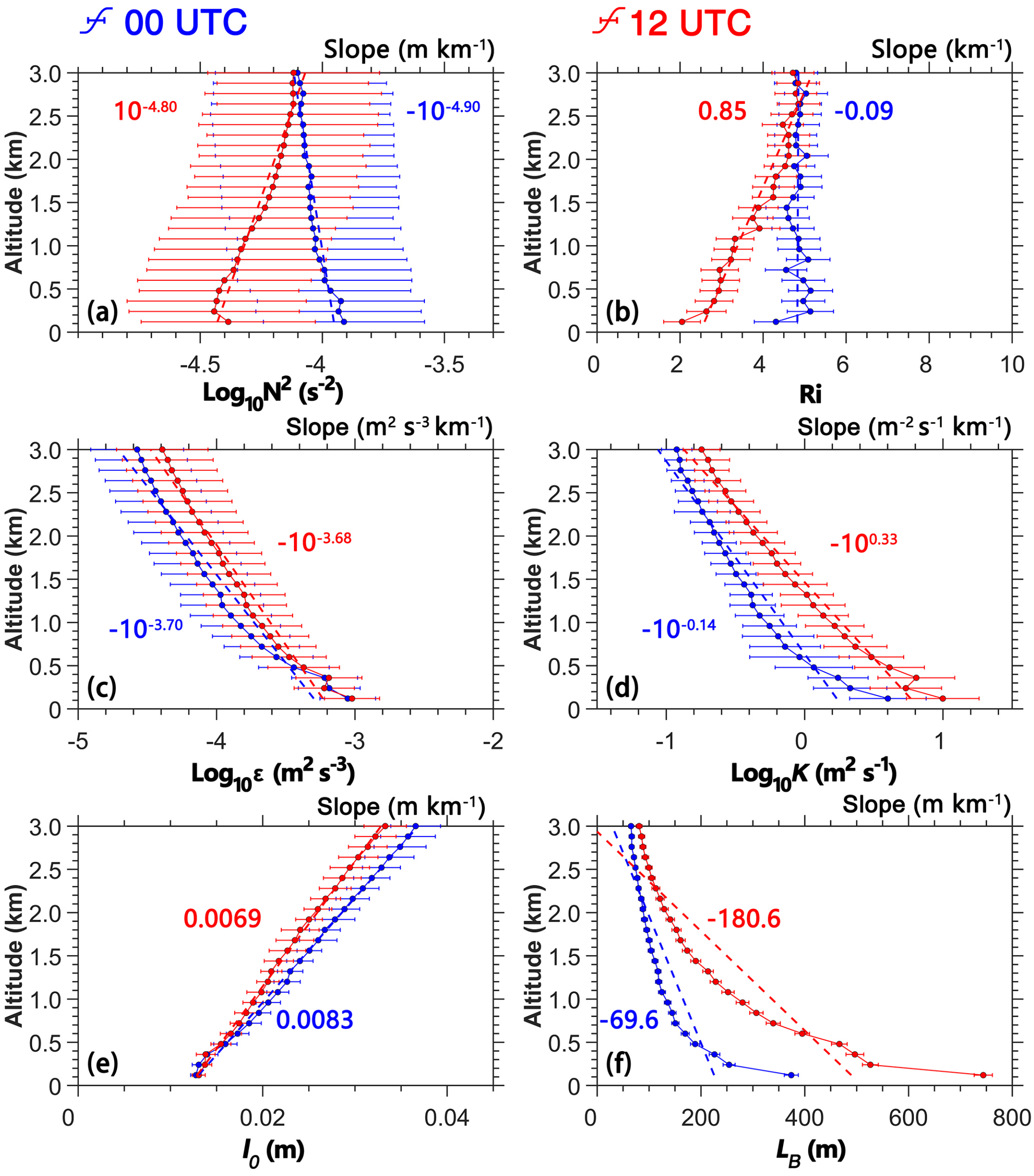

Figure 5. Vertical profiles of (a) N^2, (b) Ri, (c) ε, (d) K, (e) l_0 and (f) L_B in the 0.12 to 3.0 km altitude range AGL at 00 UTC (blue) and 12 UTC (red) for 2023, and the slope values of turbulence-related parameters with altitude are also given in each panel where red and blue values represent 00 UTC and 12UTC, respectively.

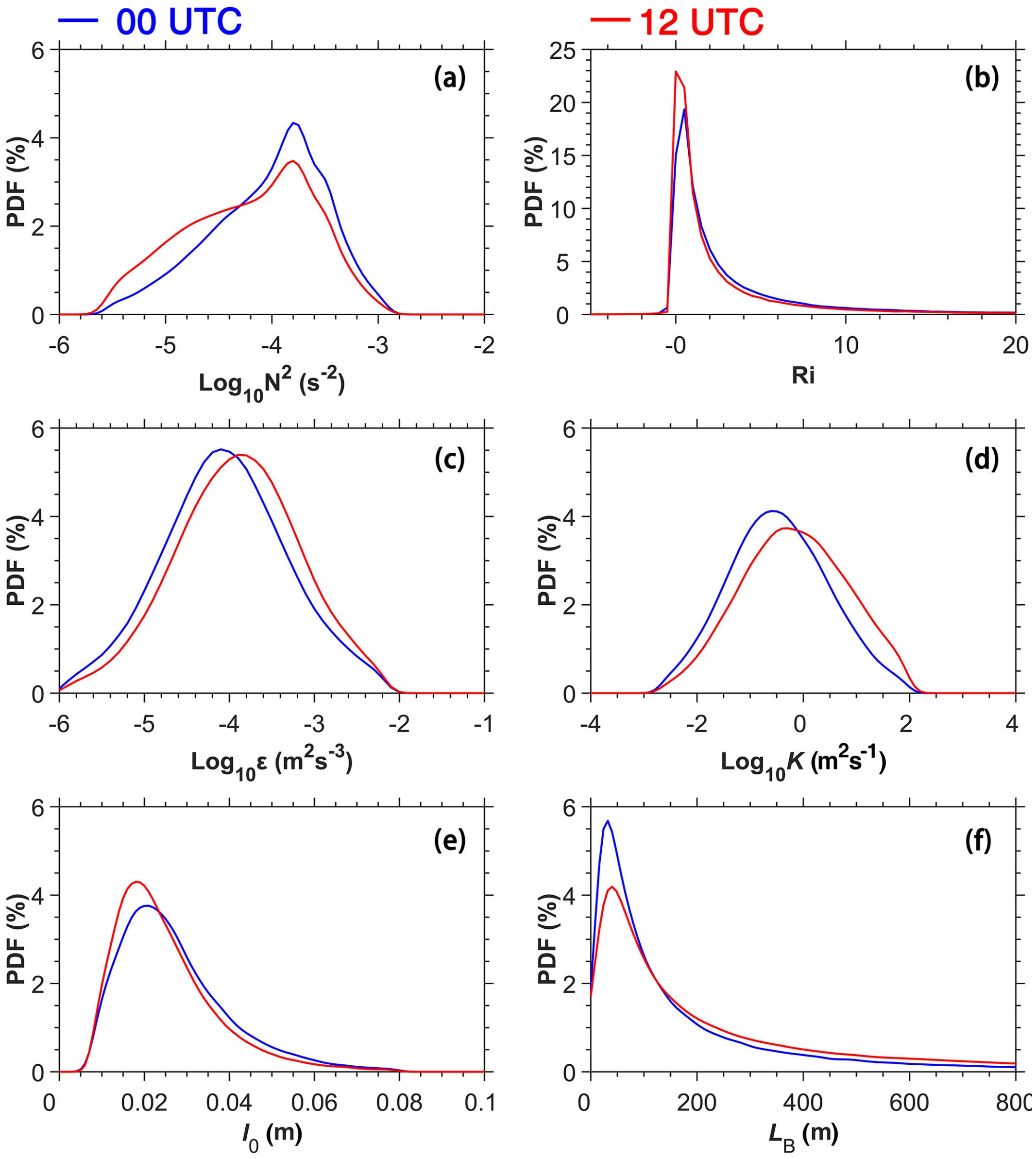

Figure 6. The probability density functions (PDF) of (a) N^2, (b) Ri, (c) ε, (d) K, (e) l_0 and (f) L_B in the 0.12 to 3.0 km altitude range AGL at 00 UTC (blue) and 12 UTC (red) for 2023, respectively.

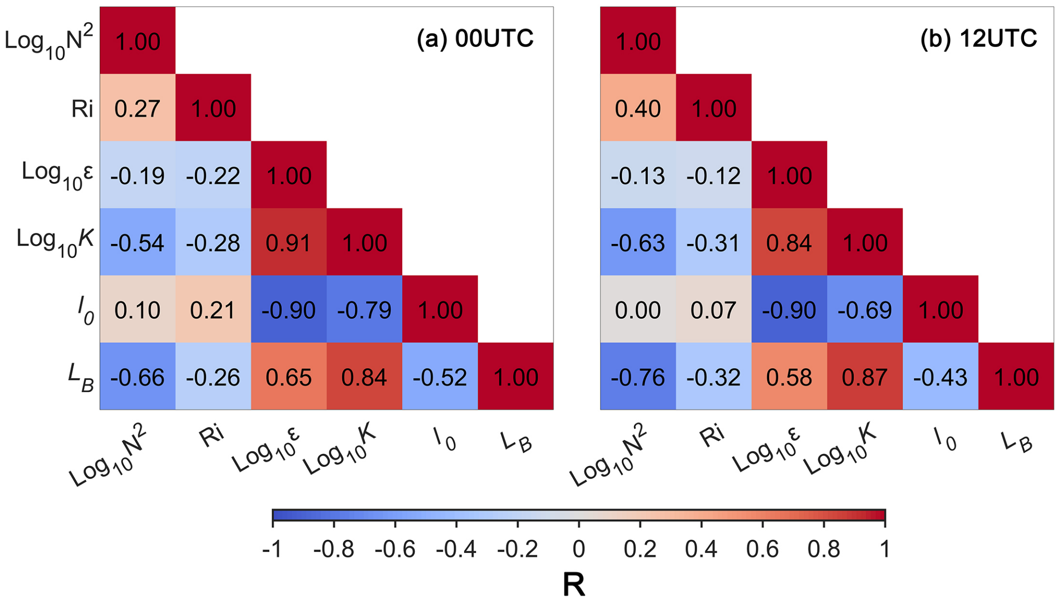

(a) 00UTC

	$Log_{10}N^2$	Ri	$Log_{10}\varepsilon$	$Log_{10}K$	l_0	L_B
$Log_{10}N^2$	1.00					
Ri	0.27	1.00				
$Log_{10}\varepsilon$	-0.19	-0.22	1.00			
$Log_{10}K$	-0.54	-0.28	0.91	1.00		
l_0	0.10	0.21	-0.90	-0.79	1.00	
L_B	-0.66	-0.26	0.65	0.84	-0.52	1.00

(b) 12UTC

	$Log_{10}N^2$	Ri	$Log_{10}\varepsilon$	$Log_{10}K$	l_0	L_B
$Log_{10}N^2$	1.00					
Ri	0.40	1.00				
$Log_{10}\varepsilon$	-0.13	-0.12	1.00			
$Log_{10}K$	-0.63	-0.31	0.84	1.00		
l_0	0.00	0.07	-0.90	-0.69	1.00	
L_B	-0.76	-0.32	0.58	0.87	-0.43	1.00

Figure 7. The correlation coefficients between turbulence-related parameters at (a) 00 UTC, (b) 12 UTC, respectively

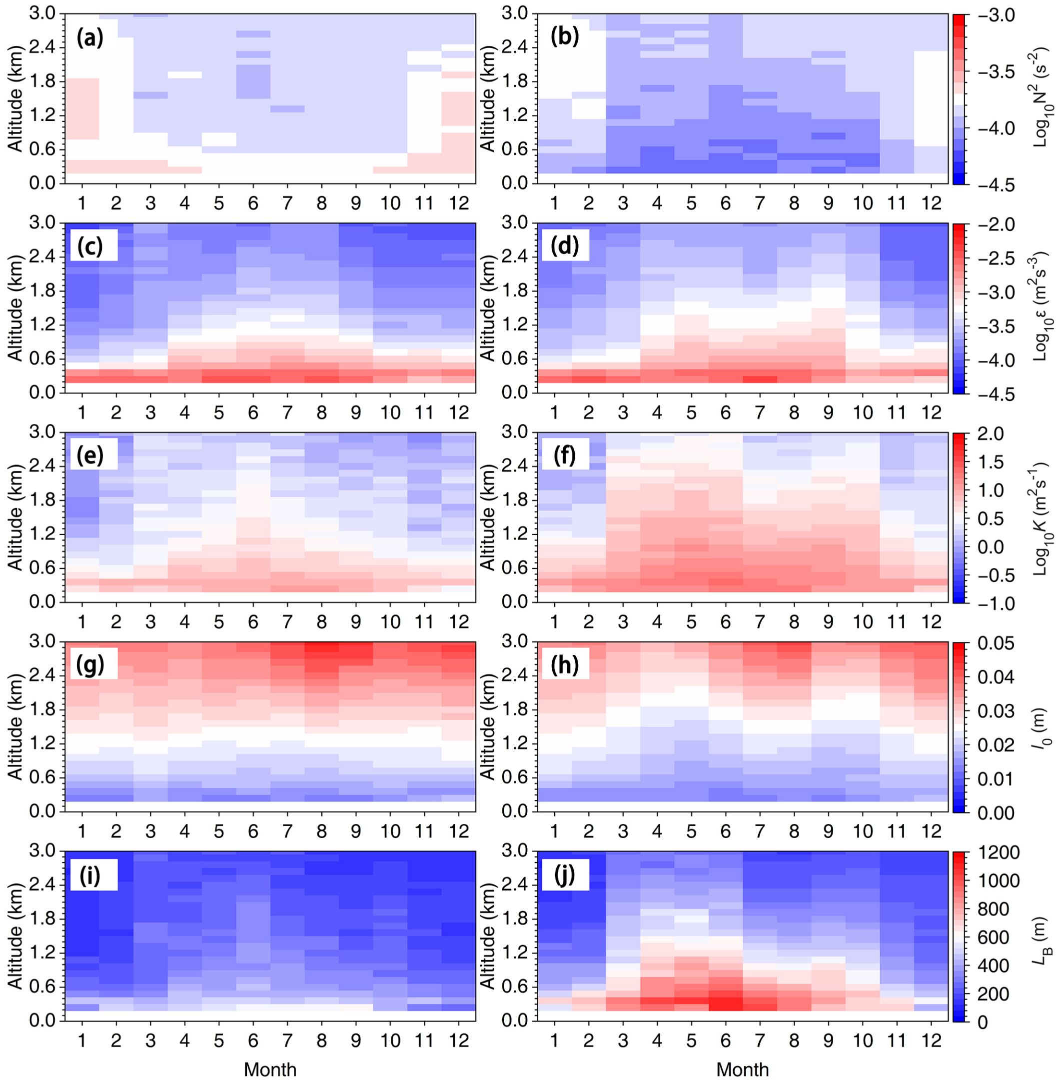

Figure 8. Monthly variation of (a) N^2, (b) Ri, (c) ε, (d) K, (e) l_0 and (f) L_B in the 0.12 to 3.0 km altitude range AGL at 00 UTC (left) and 12 UTC (right) for 2023, respectively.

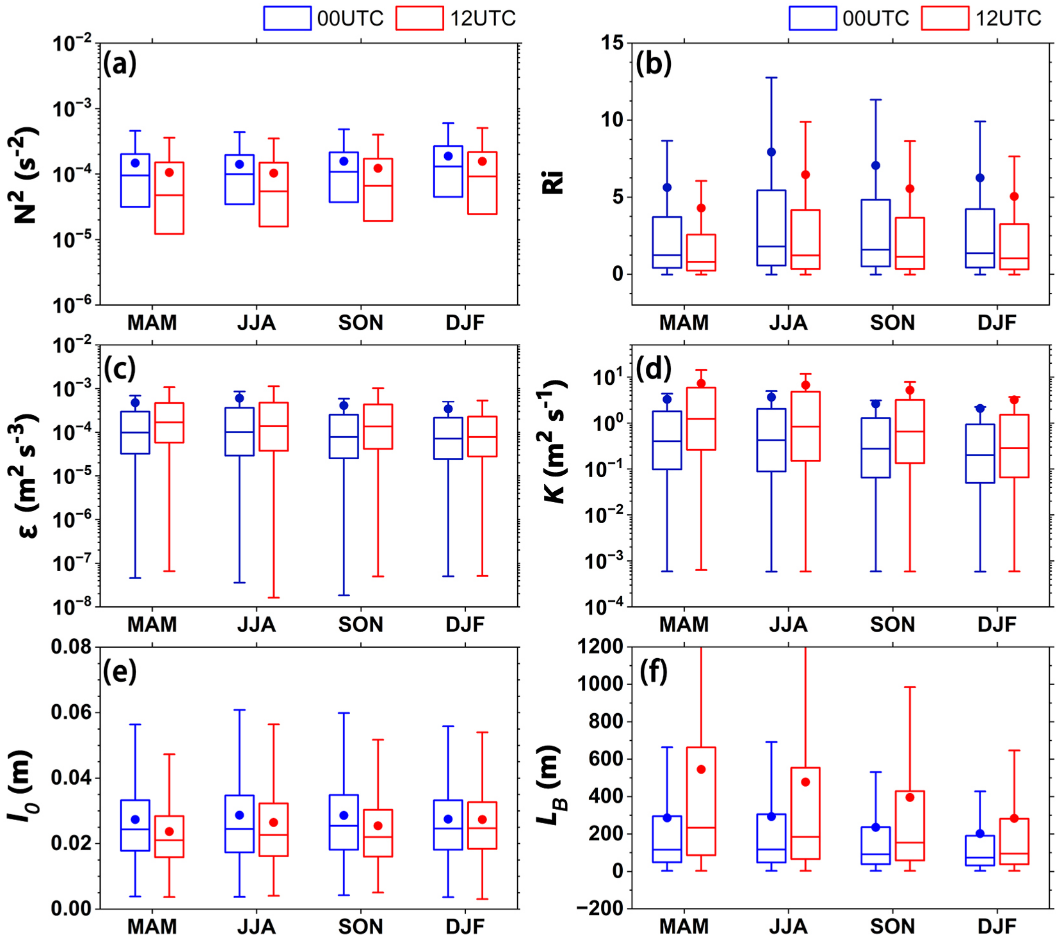

Figure 9. Box plot of seasonal (a) N^2, (b) Ri, (c) ε, (d) K, (e) l_0 and (f) L_B in the 0.12-3.0 km altitude range at 00 UTC (light blue) and 12 UTC (light red) for 2023, respectively. Note that the median is shown as a line, the mean value is displayed as a circle, whereas the outer boundaries of the boxes represent the 25th and 75th percentiles, and the lines represent the interquartile range (IQR). Seasonal divisions are MAM (March-May), JJA (June-August), SON (September-November), DJF (December-February), respectively.

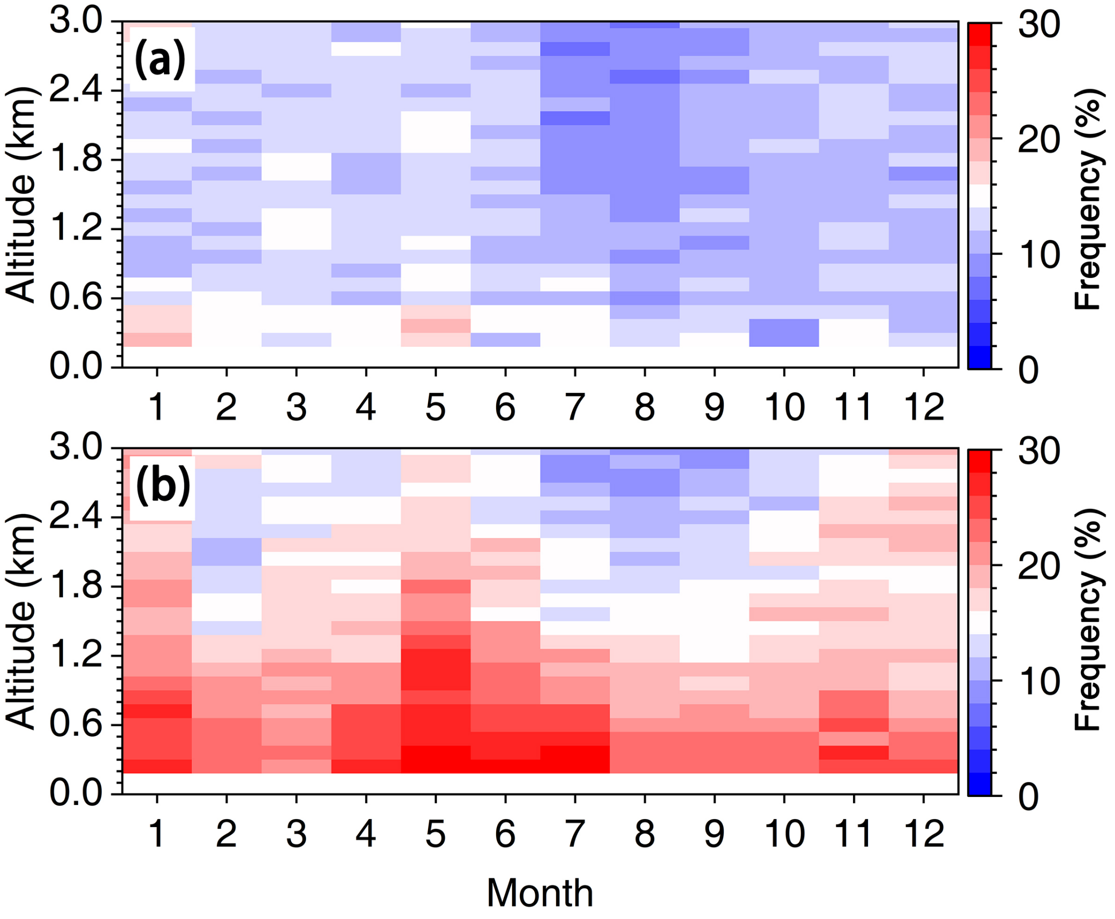

Figure 10. Monthly variation of occurrence frequency of Ri<0.25 as a function of altitude, spanning from 0.12 to 3.0 km AGL at 00 UTC (a) and 12 UTC (b) for the year of 2023, respectively.

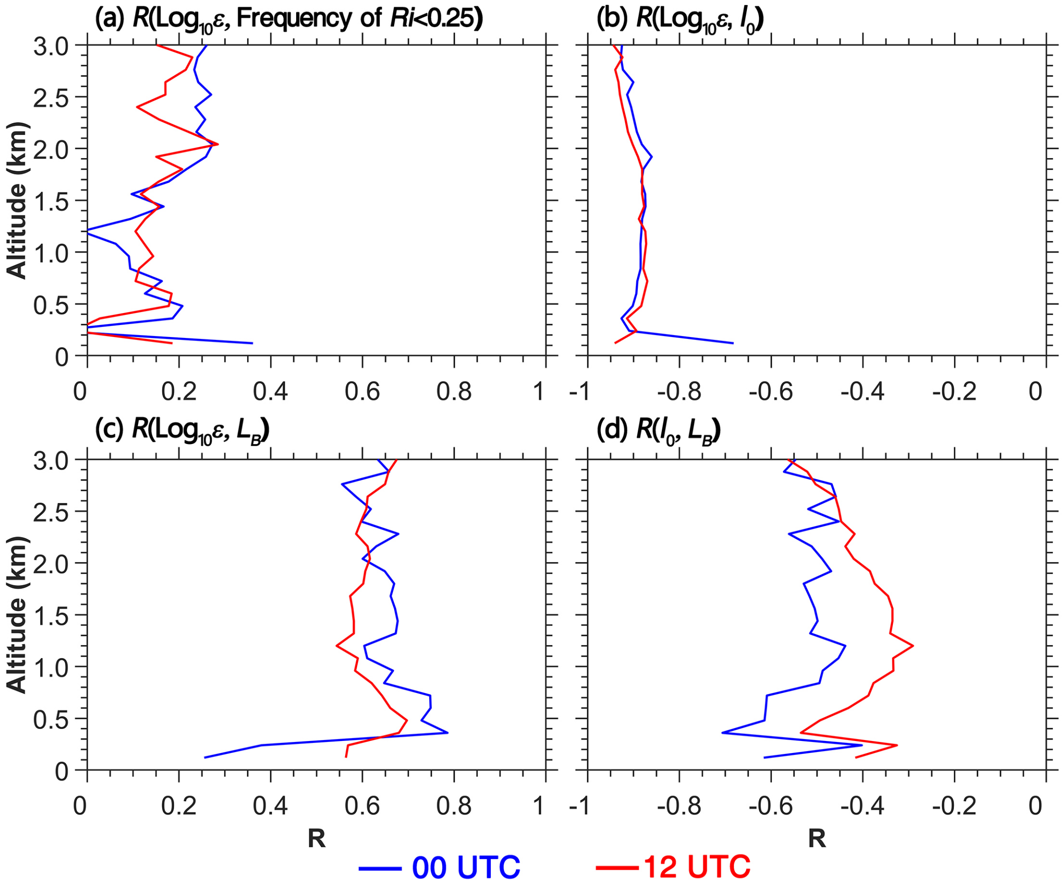

Figure 11. Profiles of correlation coefficient (R) between (a) $Log_{10}\varepsilon$ and the frequency of Ri<0.25 at 00 UTC (blue) and 12 UTC (red). (b) Same as (a) but for the correlations of $Log_{10}\varepsilon$ with l_0. (c) Same as (a) but for the correlation of $Log_{10}\varepsilon$ with L_B. (d) Correlations for l_0 and L_B in the inertial subrange, respectively.